

Early Growth in a Perturbed Universe: Dark Matter Halo Properties in 2LPT and ZA  
Simulations

By

Daniel J. Sissom

Dissertation

Submitted to the Faculty of the  
Graduate School of Vanderbilt University  
in partial fulfillment of the requirements  
for the degree of

DOCTOR OF PHILOSOPHY

in

PHYSICS

August, 2014

Nashville, TN

Approved:

Date:

---

Jocelyn K. Holley-Bockelmann, Ph.D.

---

Andreas A. Berlind, Ph.D.

---

David A. Weintraub, Ph.D.

---

Shane M. Hutson, Ph.D.

---

Robert J. Scherrer, Ph.D.

## **ACKNOWLEDGMENTS**

This is where you thank the people that made your work possible: grant awarding agencies, advisers, your committee, mom and dad, whatever.

# TABLE OF CONTENTS

	Page
<b>ACKNOWLEDGMENTS</b> . . . . .	<b>i</b>
<b>LIST OF TABLES</b> . . . . .	<b>iv</b>
<b>LIST OF FIGURES</b> . . . . .	<b>v</b>
<b>I Introduction</b> . . . . .	<b>1</b>
I.1 Simulations . . . . .	1
I.1.1 Collisionless Systems . . . . .	1
I.1.2 Collisional Systems . . . . .	1
I.1.3 Sub-grid Physics . . . . .	1
I.1.3.1 Star Formation . . . . .	1
I.1.3.2 Supernova Feedback . . . . .	1
I.1.3.3 Supermassive Black Holes . . . . .	1
I.1.3.4 Active Galactic Nuclei . . . . .	1
I.2 Simulation Initialization . . . . .	1
I.2.1 Sampling . . . . .	1
I.2.2 Displacement . . . . .	1
I.2.2.1 The Zel’dovich Approximation . . . . .	1
I.2.2.2 2nd-order Lagrangian Perturbation Theory . . . . .	1
I.3 Measurement of Dark Matter Halo Properties in Nbody Simulations . . . . .	1
I.3.1 Identifying Halos . . . . .	1
I.3.2 Density Profiles . . . . .	1
I.3.3 Concentration . . . . .	1
<b>II Computational Methods</b> . . . . .	<b>2</b>
II.1 Simulations with GADGET . . . . .	2
II.1.1 Gravity Solvers . . . . .	2
II.1.1.1 Hierarchical Tree Algorithm . . . . .	2
II.1.1.2 Particle-Mesh Algorithm . . . . .	2
II.1.2 Smoothed-Particle Hydrodynamics . . . . .	2
II.2 Finding and Measuring Dark Matter Halos with ROCKSTAR . . . . .	2
II.2.1 Algorithm . . . . .	2
II.2.2 Halo Catalogs . . . . .	2
II.3 Halo Matching with CROSSMATCH . . . . .	2
II.3.1 Particle IDs . . . . .	2

II.3.2	Algorithm . . . . .	2
<b>III</b>	<b>Supermassive Black Holes and Their Hosts . . . . .</b>	<b>3</b>
III.1	Introduction . . . . .	3
III.1.1	Galaxy Properties . . . . .	3
III.1.1.1	Color . . . . .	3
III.1.1.2	Morphology . . . . .	4
III.1.2	Supermassive Black Hole Properties . . . . .	5
III.1.3	Correlations . . . . .	8
III.1.3.1	The M-Sigma Relation . . . . .	8
III.1.3.2	The Fundamental Plane . . . . .	10
III.1.3.3	The Green Valley . . . . .	11
III.2	Galaxy Evolution . . . . .	13
III.2.1	Dark Matter Halos . . . . .	13
III.2.2	Galaxy Mergers . . . . .	14
III.3	Supermassive Black Hole Growth . . . . .	15
III.3.1	Binary Mergers . . . . .	15
III.3.1.1	Dynamical Friction and Inspiral . . . . .	15
III.3.1.2	The Final Parsec Problem . . . . .	16
III.3.1.3	Gravitational Waves and Recoil Kicks . . . . .	16
III.3.2	Accretion . . . . .	20
III.3.2.1	Bondi-Hoyle-Lyttleton Accretion . . . . .	20
III.3.2.2	Disk Accretion and Active Galactic Nuclei . . . . .	22
III.4	Conclusion . . . . .	23
III.4.1	Correlations . . . . .	23
III.4.2	Open Questions . . . . .	23
<b>IV</b>	<b>Dark Matter Halo Properties in 2LPT and ZA Simulations . . . . .</b>	<b>25</b>
IV.1	Introduction . . . . .	25
IV.2	Simulations . . . . .	26
IV.3	Analysis . . . . .	27
IV.4	Results . . . . .	28
IV.5	Discussion . . . . .	31
IV.6	Conclusion . . . . .	32
<b>V</b>	<b>Conclusion . . . . .</b>	<b>39</b>
	<b>BIBLIOGRAPHY . . . . .</b>	<b>40</b>

## LIST OF TABLES

Table

Page

## LIST OF FIGURES

Figure	Page
III.1    The Hubble tuning fork . . . . .	5
III.2    Maser orbits fit to a warped disk for NGC4258 . . . . .	7
III.3    The $M$ - $\sigma$ relation for galaxies with dynamical measurements . . . . .	9
III.4    The fundamental plane for elliptical galaxies . . . . .	11
III.5    Distribution of the fraction of galaxies containing AGN . . . . .	12
III.6    Rotation curves for 21 Sc galaxies . . . . .	13
III.7    Gravitational waveform for a black hole binary merger . . . . .	18
III.8    Gravitational wave recoil velocity from black hole mergers . . . . .	20
IV.1    Comparison of matched 2LPT and ZA halos . . . . .	34
IV.2    Histograms of $\Delta X_{\text{off}}$ . . . . .	35
IV.3    Histograms of $\Delta M_{\text{vir}}$ and $\Delta c$ . . . . .	36
IV.4 $\Delta M_{\text{vir}}$ and $\Delta c$ as a function of $M_{\text{vir,avg}}$ . . . . .	37
IV.5    Statistics for Gaussian fits . . . . .	38

# **CHAPTER I**

## **Introduction**

### **I.1 Simulations**

#### **I.1.1 Collisionless Systems**

#### **I.1.2 Collisional Systems**

#### **I.1.3 Sub-grid Physics**

##### **I.1.3.1 Star Formation**

##### **I.1.3.2 Supernova Feedback**

##### **I.1.3.3 Supermassive Black Holes**

##### **I.1.3.4 Active Galactic Nuclei**

### **I.2 Simulation Initialization**

#### **I.2.1 Sampling**

#### **I.2.2 Displacement**

##### **I.2.2.1 The Zel'dovich Approximation**

##### **I.2.2.2 2nd-order Lagrangian Perturbation Theory**

### **I.3 Measurement of Dark Matter Halo Properties in Nbody Simulations**

#### **I.3.1 Identifying Halos**

#### **I.3.2 Density Profiles**

#### **I.3.3 Concentration**

## **CHAPTER II**

### **Computational Methods**

#### **II.1 Simulations with GADGET**

##### **II.1.1 Gravity Solvers**

###### **II.1.1.1 Hierarchical Tree Algorithm**

###### **II.1.1.2 Particle-Mesh Algorithm**

##### **II.1.2 Smoothed-Particle Hydrodynamics**

#### **II.2 Finding and Measuring Dark Matter Halos with ROCKSTAR**

##### **II.2.1 Algorithm**

##### **II.2.2 Halo Catalogs**

#### **II.3 Halo Matching with CROSSMATCH**

##### **II.3.1 Particle IDs**

##### **II.3.2 Algorithm**



## CHAPTER III

### Supermassive Black Holes and Their Hosts

#### III.1 Introduction

The study of the evolution of galaxies and the growth of the supermassive black holes at their cores go hand in hand. Although the typical length scales for the two can vary by many orders of magnitude, they seem inexorably linked. Observational correlations between galaxy and supermassive black hole properties hint at an underlying co-evolution driven by shared mechanisms.

##### III.1.1 Galaxy Properties

How do we describe a galaxy? Being extended, resolvable objects, galaxies provide a unique wealth of observable characteristics not obtainable from point sources such as stars. While many characteristics can be deduced about point sources, the actual observations themselves come down to measuring position on the sky and measuring flux as a function of frequency and time. From this information, all that we know about stars and other point sources, such as temperature, age, size, and composition, can be inferred. However, for extended objects like galaxies, we are given more to work with.

##### III.1.1.1 Color

A galaxy's color is determined by its stellar component. While a galaxy in itself may be resolvable, for all but the most nearby of galaxies, individual stars are not. What we see when looking at a particular small section of a galaxy is the averaged-together light from stars in that section.

Broadly, bluer late-type spirals have a  $u - r$  color of around  $1.3 - 2.0$ , while redder early-type galaxies have a  $u - r$  color of around  $2.3 - 2.7$ . The color of a galaxy can be a good indicator for its age and evolutionary stage. Star formation processes generally tend

to produce many smaller, cooler, redder stars and fewer larger, hotter, bluer stars. These small, cool stars are much longer-lived than their massive counterparts, while the large, warm stars are much brighter. After star formation turns off, the short-lived blue stars begin to die off, and the galaxy becomes redder, as more of the fraction of total light comes from the red end of the population.

### **III.1.1.2 Morphology**

The extended nature of galaxies allows us to observe their morphology. The classification scheme originally devised by Hubble (1926) places galaxies into the four broad categories: elliptical, spiral, lenticular, and irregular. Elliptical galaxies tend to be larger, redder, have less gas, and dominated by more radial orbits. Spiral galaxies tend to be smaller, bluer, have more gas, and have more of a disk component. Spirals can have a number of arms, a central bulge, and a central bar. Lenticular galaxies are middle-of-the-road galaxies, with both a strong central bulge like an elliptical, and an extended disk like a spiral, however without spiral arms. Irregular galaxies tend to defy this simple classification scheme, and can be found in any number of configurations.

Figure III.1 is a cartoon of the classification scheme. To the left of the diagram are elliptical galaxies. The subcategories are an indication of the shape of the galaxy, with the most spherical on the left and progressing to more flattened shapes to the right. On the right of the diagram are spiral galaxies. These are broken into two branches, based on whether or not the galaxy contains a central bar. Moving from right to left, the spiral arms of the galaxies become more tightly wound, and the central bulges become more dominant. At the center of the diagram where the spiral fork meets the elliptical line, lie lenticular galaxies. Irregular galaxies are, as the name would imply, irregular and do not fall on the diagram.

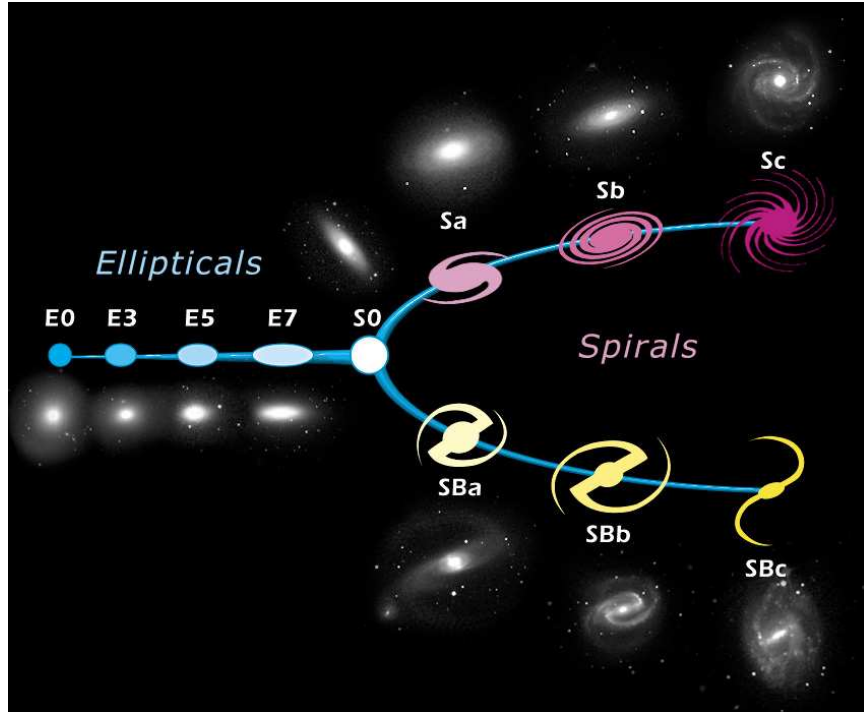


Figure III.1: The Hubble tuning fork. On the left of the diagram are elliptical galaxies. E0 galaxies are the most spherical, while E7 are the most flattened or elongated. S0 are lenticular galaxies. The top branch on the right are spiral galaxies with no bar, while the bottom right branch are spiral galaxies with a bar. Both progress from tightly wound spiral arms and large bulges to loosely wound spiral arms and small to no bulges, going from Sa to Sc or SBa to SBc.

### III.1.2 Supermassive Black Hole Properties

A non-merging black hole, much like an elementary particle, can be described simply by its mass, charge, and spin. Its effect on its local spacetime, infalling matter, and surrounding environment all come back to these three parameters. However, determination of these parameters and the study of how black holes interact with their surroundings can be quite involved.

Black holes are, by their very nature, black, and difficult to observe. We cannot see light emitted directly from a black hole as we would a star, since a black hole is defined as an object massive and compact enough to not allow light within its event horizon to escape. We are forced, therefore, to employ other methods of measuring black holes.

Thus far, the majority of progress in the measurement of black hole properties has been in measuring mass. There are a number of ways to measure the mass of a black hole. Here, we will briefly discuss masers, stellar dynamics, gas dynamics, and reverberation mapping as methods of measuring a supermassive black hole's mass.

Astrophysical masers are sources of stimulated spectral line emission in the microwave band formed in regions of high-density gas comprised of molecules such as hydroxyl, formaldehyde, and water (Lo, 2005). Since the emission frequencies of these sources are very well constrained, high-accuracy Doppler shifts can be determined. These Doppler shifts can then be used to determine velocities for the masers, and thus how much mass is enclosed by their orbits. If these masers lie very close to the supermassive black hole (SMBH) in the center of their galaxy, the enclosed mass can be constrained to be primarily that of the SMBH.

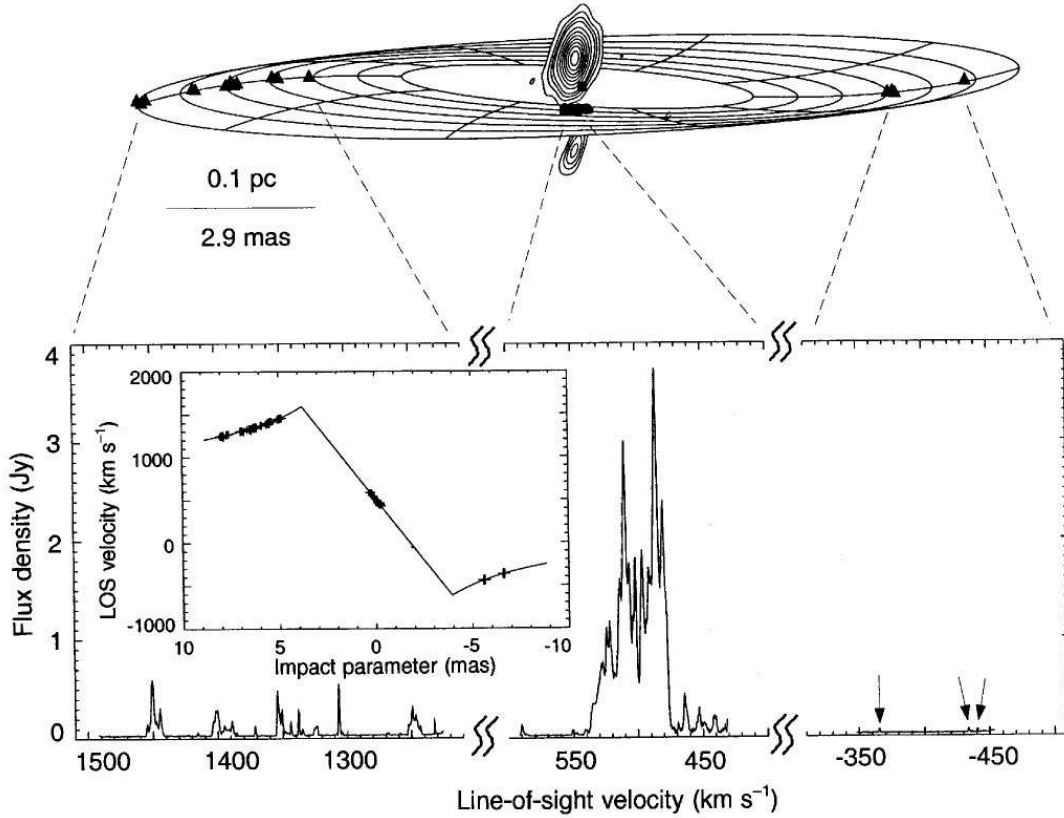


Figure III.2: Maser orbits fit to a warped disk for NGC4258. Masers can also be useful for distance determinations. Here, the positions and velocities of water masers are able to be fit to a warped disk model surrounding a supermassive black hole. This allows the interpolation of physical radii away from the black hole, giving us both the black hole mass and an standard ruler to allow precise determination of the distance to NGC4258. (Herrnstein et al., 1999)

Stellar dynamics and gas dynamics both probe light coming from matter near the black hole. The width of broadened spectral lines from either the stars or gas can be used to determine a velocity dispersion for the matter local to the SMBH. This velocity dispersion, therefore, can then be used to determine the potential through which the matter is traveling, and thus the mass of the black hole.

A special case of stellar dynamics for which the orbits of the constituent stars can be resolved—namely, for the case of our own Milky Way—adds another dimension to our knowledge of the stellar orbits. Over time, we can observe the proper motion on the sky for these orbits. Combining these measurements with Doppler measurements for radial

velocity yields full orbital solutions. Then, it simply requires Kepler’s laws to determine the mass of the SMBH.

Reverberation mapping can be thought of as “echo-mapping” the gas disk around a SMBH. Continuum emission very near the black hole travels outward and stimulates broad line emission in surrounding gas. Any changes in the continuum emission will take time to propagate to the broad line region, since the speed of light is finite. By measuring the timing difference in the change in continuum emission and change in stimulated broad line emission, the physical distance from the SMBH to the broad line region can be inferred. With this radius, and the velocity of the gas in the broad line region measured by the width of the broadened lines, a black hole mass can be determined (Blandford & McKee, 1982).

### III.1.3 Correlations

Correlations between varying properties of galaxies and black holes can provide much deeper insight into the dynamics that shape the evolution of both. Of particular interest here are the fundamental plane of elliptical galaxies, the  $M - \sigma$  relation, and the green valley-AGN relation.

#### III.1.3.1 The M-Sigma Relation

If we consider the all the observable properties of a galaxy and compare them to the mass of its SMBH, the tightest correlation can be found with the velocity dispersion  $\sigma$  of the galaxy’s bulge. Such a tight correlation is surprising, as the sphere of influence of a typical SMBH does not extend much past order a few pc, while bulges exist on scales of a kpc or greater. In essence, the supermassive black hole and the outer edges of the bulge shouldn’t “feel” each other. Nevertheless, the correlation is indeed there, suggesting some mechanism that influences—or is influenced by—both of them. Gültekin et al. (2009) use a sample of 49  $M_{BH}$  measurements and 19 upper limits to measure this correlation, and find  $\log(M_{BH}/M_{\odot}) = \alpha + \beta \log(\sigma/200 \text{ km s}^{-1})$  with  $(\alpha, \beta, \epsilon_0) = (8.12 \pm 0.08 M_{\odot}, 4.24 \pm 0.41 M_{\odot}, 0.44 \pm 0.06 M_{\odot})$  for all galaxies and  $(\alpha, \beta, \epsilon_0) = (8.23 \pm 0.08 M_{\odot}, 3.96 \pm 0.42 M_{\odot}, 0.31 \pm$

$0.06M_{\odot})$  for ellipticals, where  $\varepsilon_0$  is the intrinsic scatter in the relation.

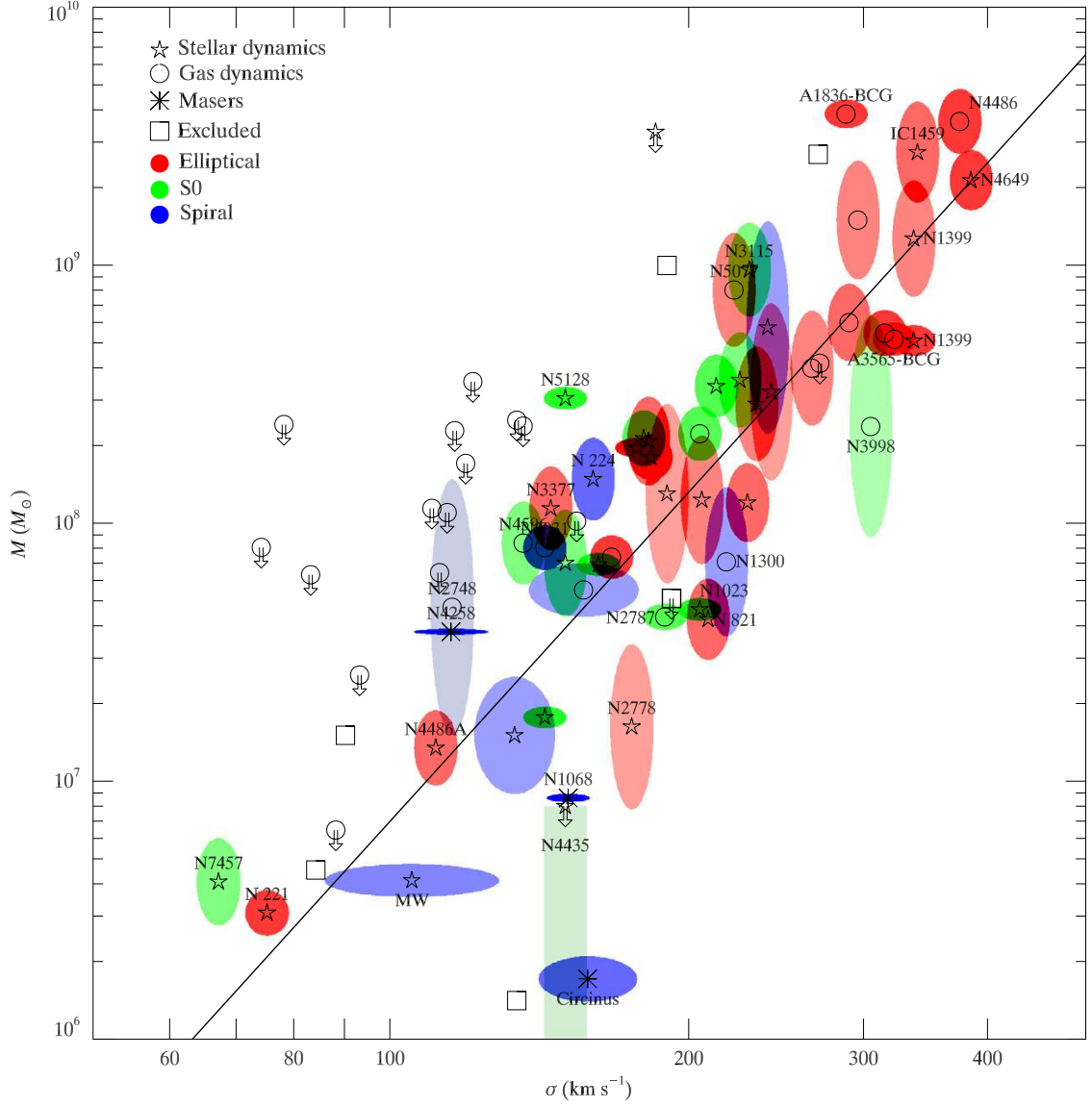


**Figure III.3:** The  $M$ - $\sigma$  relation for galaxies with dynamical measurements. Black hole mass is plotted vs velocity dispersion of its host spheroid. The symbols represent the method by which the black hole mass was measured: pentagrams for stellar dynamics, circles for gas dynamics, and asterisks for masers. Upper limits are given by arrows. Error ellipses are colored by galaxy type, with red for ellipticals galaxies, green for lenticular galaxies, and blue for spiral galaxies. The saturation of the color is inversely proportional to the area of the ellipse. For this sample, the best fit relation is  $M_{BH} = 10^{8.12} M_{\odot} (\sigma/200 \text{ km s}^{-1})^{4.24}$ . Galaxies not included in this fit are labeled as squares. (Gültekin et al., 2009)

### III.1.3.2 The Fundamental Plane

While not a direct correlation with the properties of supermassive black holes, the fundamental plane of elliptical galaxies offers insight into the characteristics of their hosts. The fundamental plane is a three-parameter correlation between properties of elliptical galaxies: velocity dispersion, effective radius, and surface brightness. This correlation (Figure III.4) between these three parameters is tighter than the combination of any two alone (Djorgovski & Davis, 1987). The fit for this correlation can be given as  $\log R_e = 0.36(\langle I \rangle_e / \mu_B) + 1.4 \log \sigma_0$ , where  $R_e$  is the effective radius in kpc,  $\langle I \rangle_e$  is the mean surface brightness interior to  $R_e$  in units of  $\mu_B$ , and  $\sigma_0$  is the velocity dispersion in  $\text{km s}^{-1}$  (Binney & Merrifield, 1998).



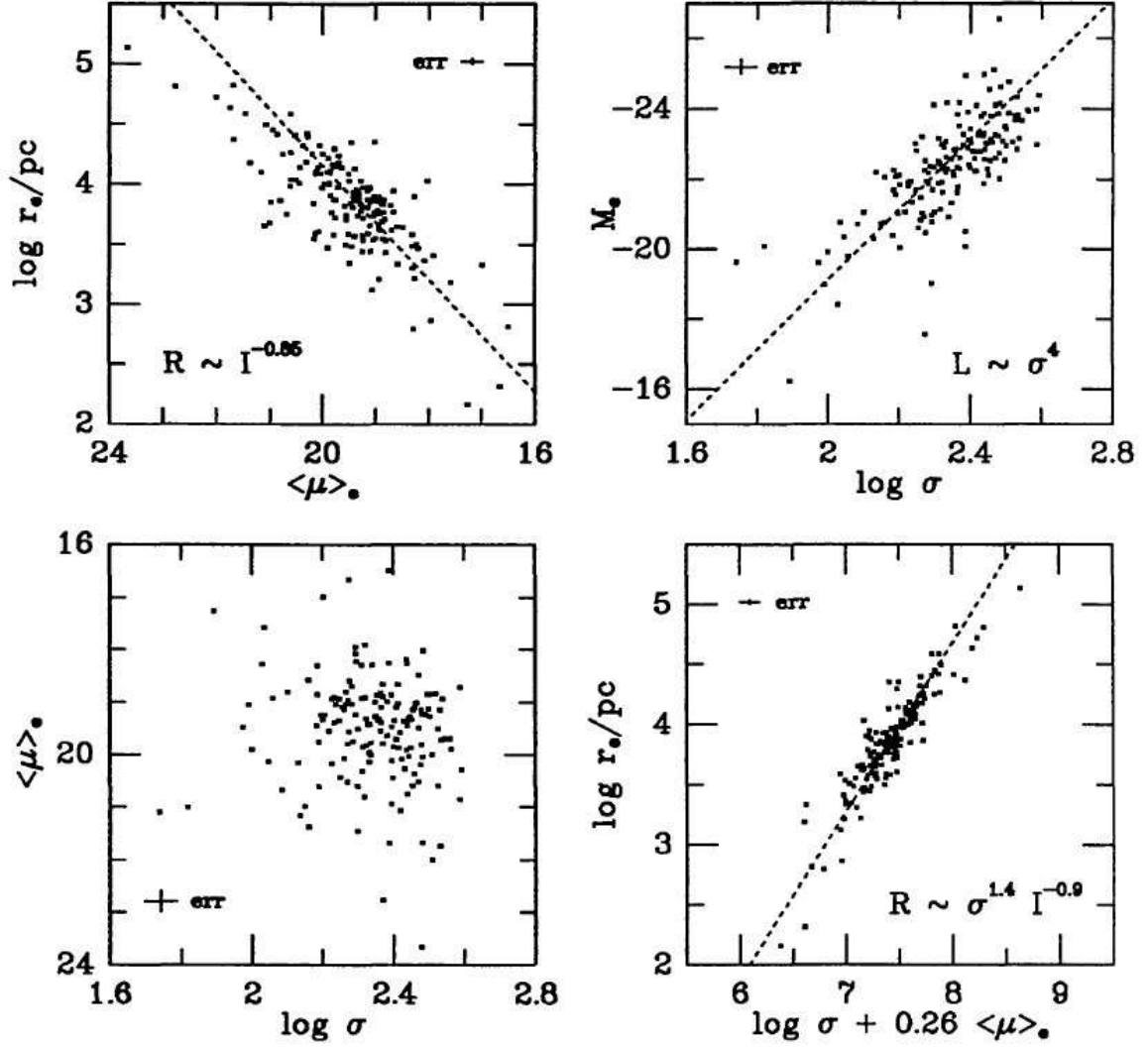


Figure III.4: The fundamental plane for elliptical galaxies. *Top panels:* The top panels show the one-parameter scaling relations, with the relation between radius and mean surface brightness on the left and the relation between luminosity and velocity dispersion (the Faber-Jackson relation) on the right. *Bottom left:* The relation between the surface brightness and velocity dispersion. This is an almost face-on view of the fundamental plane. *Bottom right:* The relation between the effective radius and the combination of surface brightness and velocity dispersion. This is the edge-on view of the fundamental plane. (Kormendy & Djorgovski, 1989)

### III.1.3.3 The Green Valley

When considering both the color and stellar mass of a galaxies, a correlation emerges where many galaxies lie in either the “blue cloud” of bluer, lower mass galaxies, or the “red

sequence” of redder, generally higher mass galaxies. The area between these two is known as the “green valley” and, while not as populated as the blue cloud or red sequence, holds special interest when active galactic nuclei (AGN) are considered. AGN are very luminous regions at the centers of some galaxies. Schawinski et al. (2010) show that galaxies falling on the green valley are much more likely to host AGN than galaxies on the blue cloud or red sequence, hinting at an underlying link between the evolution of galaxies, and the activity at their centers.

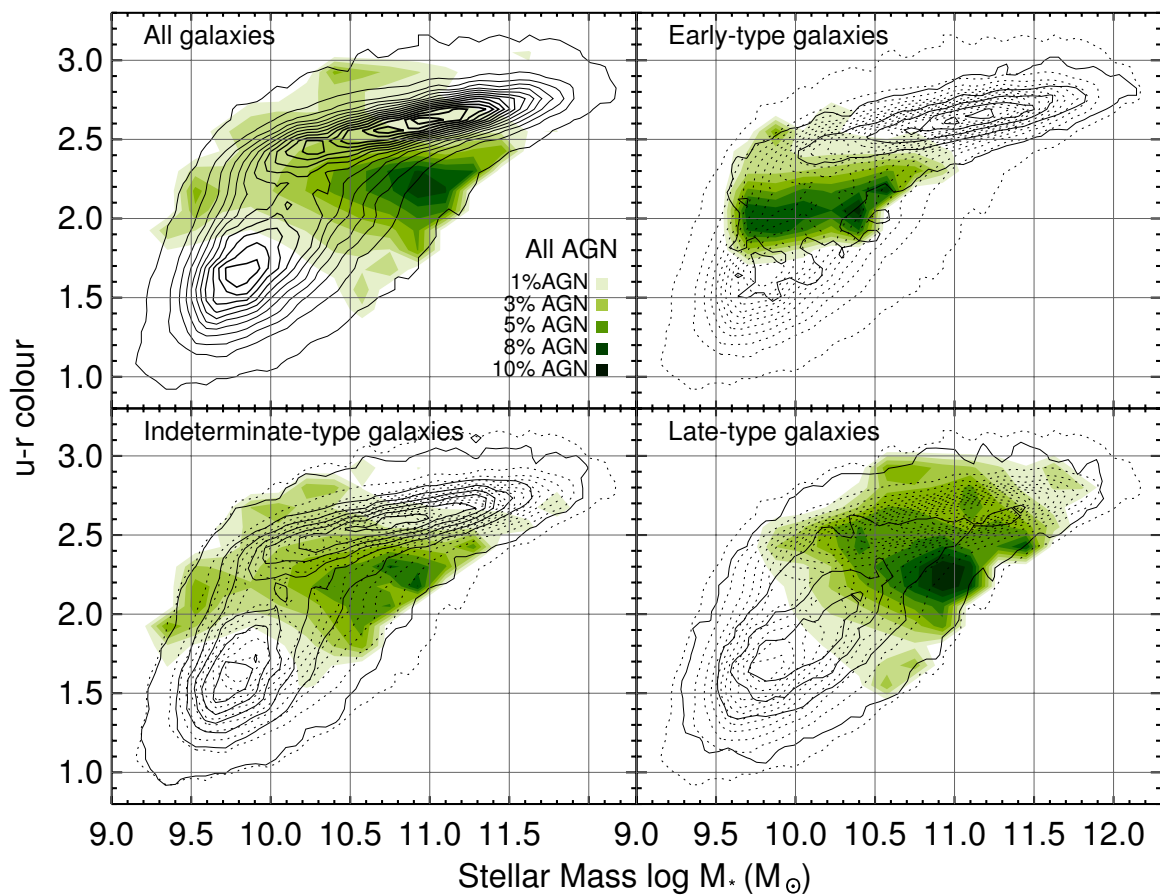


Figure III.5: Distribution of the fraction of galaxies containing AGN. Galaxy color in  $u-r$  is plotted vs stellar mass. The contours are the galaxy population for all galaxies (top-left), early-type galaxies (top right), intermediate-type galaxies (bottom left), and late type galaxies (bottom right). For the three sub-samples, dotted contours represent the full sample for comparison. The green shaded contours represent the fraction of galaxies in that subsample that contain active galactic nuclei. It can be clearly seen that the AGN fraction is highest for galaxies falling within the green valley. (Schawinski et al., 2010)

## III.2 Galaxy Evolution

### III.2.1 Dark Matter Halos

Every galaxy resides inside a dark matter halo. Often about an order of magnitude larger in both radius and mass than the baryonic component, dark matter halos dominate the large-scale behavior of galaxies. Dark matter is matter that is thought to interact very weakly or not at all with light and ordinary matter, except gravitationally. Evidence for dark matter comes from a number of sources, including the relatively flat rotational velocity curve of galaxies, the velocity dispersion of galaxies, gravitational lensing measurements, galaxy clustering, and the offset between the gas and dominant mass measured in the Bullet cluster. Here we will briefly discuss the evidence from flat rotation curves.

If there were no dark matter component and only the baryonic components (i.e. stars and gas) contributed to the galactic potential, we would expect the rotational velocity of galaxies to fall off with radius. However, observations show that the rotation curve remains relatively flat (Rubin et al., 1980). Figure III.6 shows several observed rotation curves.

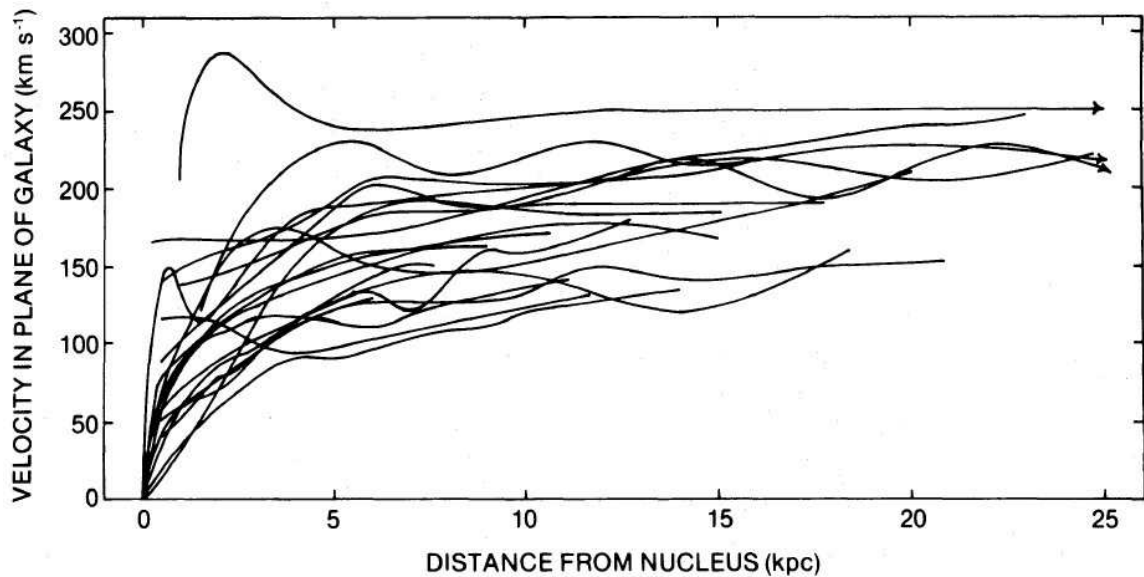


Figure III.6: Rotation curves for 21 Sc galaxies. It is readily identifiable that the rotation curves do not fall off as would be expected for galaxies without a dark matter component. (Rubin et al., 1980)

Navarro et al. (1997) found that dark matter halos generally follow the same density

profile, regardless of mass. This universal dark matter density profile can be given as

$$\rho(r) \propto \frac{1}{(r/a)(1+r/a)^2}, \quad (\text{III.1})$$

where  $a$  is the radius where the profile transitions from an  $r^{-1}$  power law to an  $r^{-3}$  power law.

### III.2.2 Galaxy Mergers

Galaxy mergers are the fundamental mechanism by which galaxies grow and evolve. Collisions between galaxies trigger processes that can alter nearly all the properties of the galaxies. Naturally, mergers increase the mass of galaxies. Starting from small perturbations in the early universe, gravity slowly pulls matter together to form larger and larger clumps. These clumps of gas and dark matter eventually form stars, beginning what we think of as typical galaxies, and over time, these galaxies merge together into larger and larger galaxies.

Mergers affect many other properties of galaxies as well. Mergers distort the shapes of galaxies, causing long tidal tails to form and the entire morphology to appear irregular. The disk structures of spiral galaxies that form from the settling of the rotational component are distorted and “puffed up” into components with ever increasing bulge-like properties.

Mergers can trigger wide-scale starburst events, where a large portion of gas goes into the formation of stars. Much of the gas component of the galaxy can subsequently be blown out by the winds from the supernovae of short-lived O and B stars. This shuts off star formation, and as the stellar population is no longer replenished with new high-mass stars, the galaxy becomes progressively redder as large stars die.

The general trend is for mergers to move galaxies from the right side of the Hubble tuning fork towards the left, turning blue, gas rich spirals into red, gas poor ellipticals. This process is aided by the AGN feedback also triggered during galaxy mergers, as we discuss in the following section.

### III.3 Supermassive Black Hole Growth

Supermassive black holes grow by two primary mechanisms, binary mergers and gas accretion. Through a combination of these, black holes can grow to as large as  $\sim 10^9\text{--}10^{10} M_\odot$  by  $z = 0$ .

#### III.3.1 Binary Mergers

When two galaxies merge, the supermassive black holes at their hearts begin a process that will eventually lead to their coalescence. There are generally thought to be three stages to this journey. First, the black holes sink towards the center of the merged galaxy through mass segregation and dynamical friction until they form a bound orbit with each other. Then, the black holes tighten their orbit through three-body scattering of nearby stars. Finally, as the black holes become close enough together for general relativistic effects to come into play, gravitational waves are emitted and radiate away the remaining orbital energy until the binary coalesces.

##### III.3.1.1 Dynamical Friction and Inspiral

During the majority of the inspiral process, the black holes do not “feel” each other’s gravitational pull. Instead, interactions with the galaxy itself push the holes together.

As it travels through a galaxy, a black hole—or any massive body—is slowed by the surrounding field of matter. Gravitational attraction pulls surrounding matter toward the black hole. However, as the black hole is moving with respect to the local medium, the attracted particles will tend to fall behind the black hole. This creates a wake of overdensity that gravitationally attracts the black hole from behind and slows its velocity. Chandrasekhar (1943) develops this notion of dynamical friction for the motion of a star through a sea of other stars. If the distribution of velocities of the surrounding particles is Maxwellian, the acceleration on the black hole can be written as

$$\frac{d\mathbf{v}_M}{dt} = -\frac{4\pi G^2 M \rho \ln \Lambda}{v_M^3} \left[ \text{erf}(X) - \frac{2X}{\sqrt{\pi}} e^{-X^2} \right] \mathbf{v}_M, \quad (\text{III.2})$$

where  $v_M$  is the velocity of the black hole,  $M$  is its mass,  $\rho$  is the density of surrounding matter,  $\text{erf}$  is the error function,  $\ln \Lambda$  is the Coulomb logarithm, and  $X \equiv v_M/(\sqrt{2}\sigma)$  where  $\sigma$  is the velocity dispersion of the surrounding medium (Binney & Tremaine, 1988). As the black hole is slowed by dynamical friction, it loses angular momentum and sinks towards the center of the galaxy’s potential well.

### **III.3.1.2 The Final Parsec Problem**

Dynamical friction and mass segregation can only take us so far. Once the black holes are close enough together, they form a bound binary orbit. This generally occurs for separations of around a few to tens of parsecs. This presents a problem, however, since the orbit needs to shrink to around  $10^{-2}$ – $10^{-3}$  pc in order for gravitational wave emission to remove energy from the orbit in a significant amount. The orbit can be tightened with three-body scattering of stars that wander through the orbit of the binary, however, in the spherical galaxies where mergers often take place, there is a depletion of stars with orbits that intersect the binary. Khan et al. (2011), however, show that the non-spherical, triaxial potential typical of post-merger galaxy remnants can efficiently funnel stars through the orbit of the black hole binary with sufficient intensity to tighten the binary orbit to the gravitational wave regime.

### **III.3.1.3 Gravitational Waves and Recoil Kicks**

Once the black hole binary separation reaches the point where strong field general relativistic effects come into play, we no longer require external influences to nudge the black holes together. In the final plunge toward coalescence, the black hole binary sheds energy through emission of gravitational radiation. As energy is radiated away, the binary tightens its orbit until the two black holes merge into one. Following this coalescence, the resultant black hole undergoes a “ringdown” phase, in which the distorted space time settles back down into a black hole that can again be simply described by mass, charge, and spin.

The emission of gravitational waves has two interesting consequences. First, the radiation from two merging supermassive black holes is extremely loud, and can potentially

provide an observational signature of the process for gravitational wave observatories. Second, the gravitational waves carry linear momentum, leading to a recoil “kick” imparted to the black hole merger remnant.

Recent advances in numerical relativity simulations have provided a much deeper insight into the black hole binary merger process than has been previously available. Waveforms produced from these simulations (Figure III.7) can be used to predict what gravitational wave observatories such as LIGO and LISA would expect to observe for signals originating from merging supermassive black hole binaries. Having these waveforms as templates for comparison to data can greatly increase the signal to noise ratio for these detectors, potentially allowing the gravitational wave events to be seen among the sea of noise. These waveforms produced from simulations of the last few orbits of inspiral through the merger and ringdown can be combined with waveforms suggested from post-Newtonian approximations for the longer duration inspiral to provide a complete extended signal to match against.

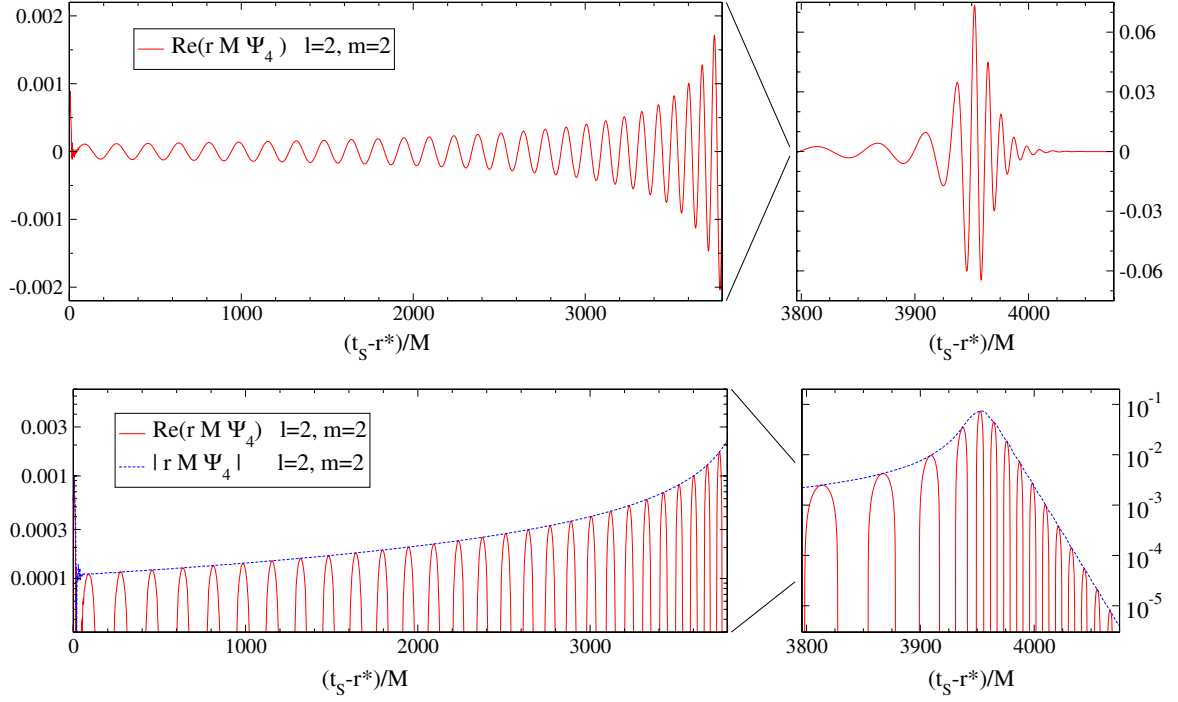


Figure III.7: Gravitational waveform for an equal-mass, non-spinning black hole binary merger. This is the final waveform, extrapolated to infinity, from the numerical relativity simulation of Scheel et al. (2009). The waveform is shown on the top panel with a linear y-axis and on the bottom panel with a logarithmic y-axis. The left panels are the earlier stages of inspiral, and the right panels show the merger and ringdown stages.

For asymmetric mergers, gravitational radiation is emitted anisotropically. This causes a recoil kick, in which the gravitational waves impart a net velocity to the final black hole with respect to the original center of mass. The magnitude and direction of this kick are dependent on the mass ratio of the binary and the spins of the two black holes—in all, a 7-dimensional parameter space. This large parameter space has been largely explored with numerical relativistic simulations, and analytic equations can be fit to the data to predict the recoil from a given merger configuration. Holley-Bockelmann et al. (2008), give these equations as

$$\mathbf{v}_{kick} = (1 + e) \left[ \hat{\mathbf{x}}(v_m + v_\perp \cos \xi) + \hat{\mathbf{y}}v_\perp \sin \xi + \hat{\mathbf{z}}v_\parallel \right], \quad (\text{III.3})$$



where

$$v_m = A \frac{q^2(1-q)}{(1+q)^5} \left[ 1 + B \frac{q}{(1+q)^2} \right], \quad (\text{III.4})$$

$$v_\perp = H \frac{q^2}{(1+q)^5} \left( \alpha_2^\parallel - q \alpha_1^\parallel \right), \quad (\text{III.5})$$

$$v_\parallel = K \cos(\Theta - \Theta_0) \frac{q^2}{(1+q)^5} \left( \alpha_2^\perp - q \alpha_1^\perp \right). \quad (\text{III.6})$$

Here, the fitting constants are  $A = 1.2 \times 10^4 \text{ km s}^{-1}$ ,  $B = -0.93$ ,  $H = (7.3 \pm 0.3) \times 10^3 \text{ km s}^{-1}$ , and  $K = (6.0 \pm 0.1) \times 10^4 \text{ km s}^{-1}$ . The  $\hat{z}$  unit vector is in the direction of the orbital angular momentum, and  $\perp$  and  $\parallel$  refer to components perpendicular and parallel to  $\hat{z}$ , respectively. The fitting parameters are the eccentricity  $e$ , the mass ratio  $q \equiv M_2/M_1$ , and the reduced spin parameters  $\alpha_i \equiv S_i/M_i^2$  where  $S$  is the spin angular momentum. The orientation of the merger is given by the angles  $\Theta$ ,  $\Theta_0$ , and  $\xi$  (Holley-Bockelmann et al., 2008).

Slices through this parameter space are shown in Figure III.8. For certain configurations of the merger, the recoil velocity can be very high. Very asymmetric mergers can produce recoils as high as  $\sim 4000 \text{ km s}^{-1}$ . These large recoils can be enough for the black hole to escape the potential well of its host galaxy and be ejected. Even less extreme recoil kicks can affect the evolution of black holes, as the kicked black hole can oscillate about its host's center, potentially changing its local gas environment and accretion rate.

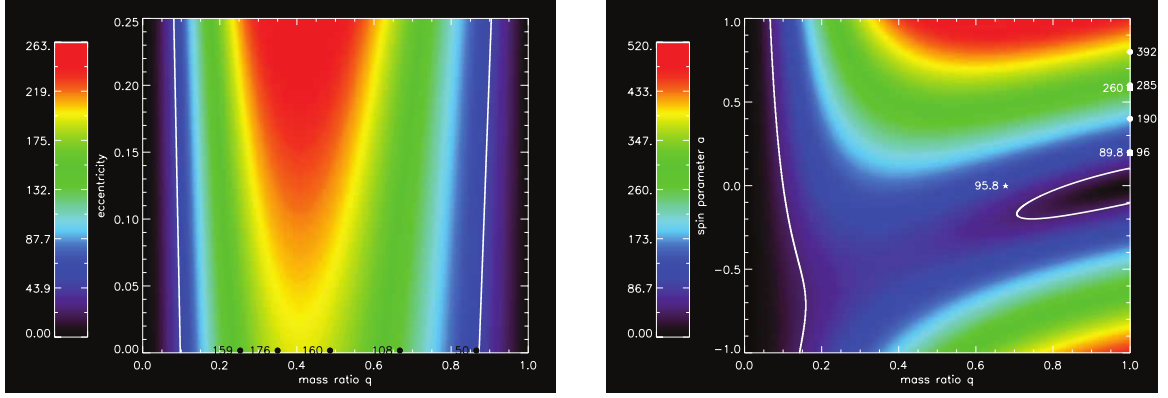


Figure III.8: *Left:* Gravitational wave recoil velocity from a merger of nonspinning black holes as a function of eccentricity and mass ratio. Data from numerical relativity simulations (González et al., 2007) are overlaid along the zero eccentricity line. The overlaid white contours are the escape velocity of a typical globular cluster,  $50 \text{ km s}^{-1}$ . *Right:* Gravitational wave recoil kick velocity as a function of spin parameter and mass ratio for a merger of spinning black holes on a circular orbit with spins perpendicular to the orbital plane of the binary and anti-aligned with each other. Again, the  $50 \text{ km s}^{-1}$  escape velocity of a globular cluster is overlaid as white contours. Results from numerical relativity simulations are over-plotted: squares for Koppitz et al. (2007), circles for Herrmann et al. (2007), and star for Brüggmann et al. (2004). (Holley-Bockelmann et al., 2008)

### III.3.2 Accretion

Although mergers play an important role in the evolution of supermassive black holes, gas accretion can often dominate in terms of mass growth. Gas can fall into a black hole in a number of ways. Here, we will discuss accretion onto a moving black hole, spherical accretion onto a stationary black hole, and disk accretion onto a stationary black hole.

#### III.3.2.1 Bondi-Hoyle-Lyttleton Accretion

Let us first consider a massive object, in this case our black hole, moving through a uniform density gas medium. Just as in the case of dynamical friction, particles close enough to the black hole will feel a gravitational attraction, causing them to move toward the black hole. As they move closer, the black hole is also moving through the medium, causing the gas particles to focus behind the black hole. As the particle stream reaches the wake directly

behind the black hole, it collides with opposing streams, causing the angular momentum to go to zero. If these particles are bound, they will proceed to fall onto the black hole. Hoyle & Lyttleton (1939) derive an impact parameter for which particles will be accreted,

$$\sigma < \sigma_{HL} = \frac{2GM}{v_\infty^2}, \quad (\text{III.7})$$

and a mass accretion from the wake column at a rate of

$$\dot{M}_{HL} = \pi \sigma_{HL}^2 v_\infty \rho_\infty = \frac{4\pi G^2 M^2 \rho_\infty}{v_\infty^3}, \quad (\text{III.8})$$

where  $v_\infty$  and  $\rho_\infty$  are the velocity and density far away from the black hole, respectively. Expanding upon this analysis, Bondi & Hoyle (1944) suggest that the accretion rate should rather be

$$\dot{M}_{BH} = \frac{2\alpha \pi G^2 M^2 \rho_\infty}{v_\infty^3}, \quad (\text{III.9})$$

where  $\alpha$  is a constant between 1 and 2, with a typical value of around 1.25.

For an accretor at rest in an isotropic gas medium, one would expect accretion to be a spherical process. Bondi (1952) considers this configuration, and finds the accretion rate for this “temperature-limited” case to be

$$\dot{M}_{Bondi} = \frac{2\pi G^2 M^2 \rho_\infty}{c_{s,\infty}^3}, \quad (\text{III.10})$$

where  $c_{s,\infty}$  is the speed of sound far away from the black hole.

Extrapolating between this result and the “velocity-limited” case of Equation III.9 suggests (Bondi, 1952)

$$\dot{M}_{BH} = \frac{2\pi G^2 M^2 \rho_\infty}{(c_{s,\infty}^2 + v_\infty^2)^{3/2}} \quad (\text{III.11})$$

as an order of magnitude estimate of the more general case of accretion. Numerical simulations (Shima et al., 1985) suggest an additional factor of 2 is needed for better agreement

with simulation results, giving us a generally applicable formula for the accretion rate,

$$\dot{M}_{BH} = \frac{4\pi G^2 M^2 \rho_\infty}{(c_{s,\infty}^2 + v_\infty^2)^{3/2}}. \quad (\text{III.12})$$

### III.3.2.2 Disk Accretion and Active Galactic Nuclei

Active galactic nuclei play a fundamental role in the evolution of both supermassive black holes and their host galaxies. As gas falls in to a black hole in the center of a galaxy, its angular momentum forces it into an accretion disk. As matter moves towards the SMBH, it transfers its gravitational potential energy to thermal energy. For accretion disks around supermassive black holes, this can cause the disk to emit large amounts of electromagnetic radiation (Lin & Papaloizou, 1996).

This emitted radiation is important in a number of ways. Most critical to the SMBH itself is the radiation pressure exerted on infalling matter. This radiation pressure sets an upper limit on the rate of accretion, as there is a point where the force from emitted radiation balances the force of gravity for infalling gas (Rybicki & Lightman, 1979). This limit, known as the Eddington limit, is given by

$$L_{Edd} = 4\pi G M c m_H / \sigma_T = 1.25 \times 10^{38} \text{erg s}^{-1} (M/M_\odot), \quad (\text{III.13})$$

where  $c$  is the speed of light,  $m_H$  is the mass of hydrogen, and  $\sigma_T$  is the Thompson cross section.

The radiation given off by the accretion disk affects galactic properties as well. Powerful AGN can strip away gas from the center of the galaxy, halting star formation. This can quickly change a galaxy from a blue, gaseous, star forming galaxy into one that is red, dry, and dead.

### III.4 Conclusion

We have seen that galaxies and the supermassive black holes at their centers both have their most dramatic periods of evolution around the same time. Galaxy mergers grow both the galaxy and the SMBH. Galaxies grow and become more elliptical as mergers bring in additional mass on orbits that can disrupt their gaseous disks. These mergers also bring in counterpart supermassive black holes that fall toward the center of the galaxy and merge with the central SMBH, while also triggering accretion events and AGN feedback that pump energy back into the galaxy, shutting off star formation.

#### III.4.1 Correlations

In light of these shared growth mechanisms, the correlations mentioned in Section IV.1 begin to move from a purely observational coincidence to a natural result of co-evolution. The  $M-\sigma$  relation is a natural byproduct of the simultaneous growth of supermassive black holes and their galaxies during merger events. The mass of the SMBH increases due to the merging of binary companions and increased levels of accretion, while the host mass, and thus velocity dispersion, increases due to the infalling galaxy itself. Likewise, the overabundance of AGN in galaxies lying in the green valley is the consequence of simultaneous change. Mergers both trigger highly luminous AGN feedback and cause an inexorable shift from the blue cloud, through the green valley, to the red sequence. Even the increase in scatter of the  $M-\sigma$  relation at low masses can be explained by the galaxies having lower mass, and therefore being more likely to allow a gravitational wave recoil kicked black hole of a given velocity to escape.

#### III.4.2 Open Questions

In the end, there remain a number of open questions. How can very large supermassive black holes form so early? What is dark matter actually made of? How do galaxies retain their black holes if merger recoils can kick them with velocities greater than the escape velocity of the galaxy? Over what range are our correlations truly valid? These are just

some of the questions that are currently being investigated, and promise to provide a rich field of study for years to come.

## CHAPTER IV

### Dark Matter Halo Properties in 2LPT and ZA Simulations

#### IV.1 Introduction

Dark matter halo evolution in the early universe during the pre-reionization Dark Ages plays a pivotal role in shaping the properties of these halos both early in their evolution and at later redshift. During these early times, small overdensities in the relatively smooth background of dark matter begin the collapse leading to virialized halos. In cosmological N-body simulations, these initial overdensities are often on the order of numerical noise, and difficult to simulate directly. Displacement field techniques are often used to nudge particles from their initial positions to an approximation of where they should be at a more reasonable starting redshift. However, bulk halo properties at later redshift can be sensitive to deviations in this initial displacement. In this paper, we explore dark matter halo populations in simulations with two different initialization techniques and compare the effect of initialization on halo properties as a function of redshift during the Dark Ages.

At high redshift, in the so-called Dark Ages before reionization, dark matter (DM) halos undergo a significant amount of growth. This growth, whether due to mergers or accretion, plays a pivotal role in shaping a halo's properties. During this time of early growth, smaller variations in a halo's growth history can lead to large bulk property changes. A number of studies explore halo growth at lower redshift<sup>[citation needed]</sup>, but fewer consider the high redshift regime<sup>[citation needed]</sup>.

Cosmological simulations that follow the initial collapse of dark matter density peaks into virialized halos often neglect to consider the nuances of initialization method. While differences in ensemble halo properties between simulation initialization methods, such as the halo mass function, are mostly washed away by  $z = 0$ <sup>[citation needed]</sup>, trends at earlier redshifts are less studied.

Starting a simulation directly from the redshift of the initial conditions provided by surface of last scattering data proves impractical, as initial density peaks at this time are on the order of numerical noise of the simulation. Starting at a later redshift saves computation time as well as avoiding the errors introduced by simulating noise. The usual procedure is to apply a displacement field to the initial particle positions and evolve them semi-analytically to the starting redshift of the numerical simulation.

In this paper, we compare the Zel’dovich approximation with 2nd-order Lagrangian Perturbation Theory for initial particle displacement. The Zel’dovich approximation (ZA, hereafter) is a linear displacement field, while 2nd-order Linear Perturbation Theory (2LPT, hereafter) adds a second-order correction term to the expansion. 2LPT allows for a later starting redshift compared with an equivalent ZA–initialized simulation. However, many ZA simulations do not take this into account, starting from too late of an initial redshift<sup>[citation needed]</sup>.

It is thought that 2LPT allows initial DM overdensities to get a “head start” compared with ZA, allowing earlier structure formation, more rapid evolution, and larger possible high–mass halos for a given redshift. We explore this possibility by comparing halo properties in (otherwise identical) simulations initialized with ZA and 2LPT.

We discuss the simulations in §IV.2, halo finding and analysis methods in §IV.3, results in §IV.4, implications and future work in §IV.5, and finally summarize and conclude in §IV.6.

## IV.2 Simulations

We use the Nbody tree/SPH code GADGET-2 (Springel, 2005) to evolve six dark matter–only cosmological volumes from  $z_{start} = 300$  to  $z = 6$  in a  $\Lambda$ CDM universe. Each simulation is initialized using WMAP–5 parameters. For each of the three simulation pairs, we directly compare 2LPT and ZA by identically sampling the CMB transfer function and displacing the initial particle positions to the same starting redshift using 2LPT and ZA. The three sets of simulations differ only by the initial phase sampling random seed.



Each volume contains  $512^3$  particles in a  $10 h^{-1}$  Mpc box. For full simulation details, see Holley-Bockelmann et al. (2012).

### IV.3 Analysis

For each of our six simulations, we use the 6-D phase space halo finder code ROCKSTAR to identify spherical overdensity halos at each timestep. ROCKSTAR follows an adaptive hierarchical refinement of friends-of-friends halos in 6-D phase space<sup>[citation needed]</sup>, allowing determination of halo properties such as constituent friends-of-friends particles, particles within the virial radius, halo mass, position, virial radius, internal energy, and substructure. ROCKSTAR claims to be able to track halos down to a threshold of around 20 particles<sup>[citation needed]</sup>, but we use a more conservative 100 particle threshold for our analysis. We use all particles found within the virial radius to define our halos and their properties.

We match halos between companion simulations with our CROSSMATCH code<sup>[citation needed]</sup>. Each pair of simulations is initialized with the same particle ID scheme, so that a given particle ID corresponds to the same particle in each simulation. This allows us to match particle-to-particle between the simulations and identify matching halos based on the highest fraction of matching particles contained in each at any given timestep. Add sentence about “best matching” and existence of match in both directions. We find, for example, matches for about xx% of halos above our particle count threshold at  $z = 6$ . With halo catalogues matched between simulations, we can compare properties of individual corresponding halos. We “stack” the three simulation boxes for each initialization method, and combine the halos from each into one larger sample in our analysis.

Halo concentration  $c = R_{vir}/R_s$  is derived from ROCKSTAR’s output for  $R_s$  and  $R_{vir}$ , where  $R_s$  is the scale radius defined by the NFW<sup>[citation needed]</sup> profile

$$\rho(r) = \frac{\rho_0}{\frac{r}{R_s} \left(1 + \frac{r}{R_s}\right)^2} \quad (\text{IV.1})$$

and  $R_{vir}$  is the virial radius as defined by Bryan & Norman (1998).

To verify the accuracy of the ROCKSTAR fit, we independently find density profiles for several halos and compare the fit parameters such as  $R_s$ . For each halo, we fit an NFW density profile to logarithmic radial bins of particle position with a non-linear least squares fitting routine from the SciPy library. From this, we measure the scale radius and, along with virial radii from ROCKSTAR, the concentration. The bottom two rows of Figure IV.1, for example, show the fitting results for a particle matched halo pair. For halos fit by our method, our results are in relatively good agreement with ROCKSTAR. However, as we do not find an acceptable fit for every halo, we use the more complete ROCKSTAR data for the final concentration measurements.

#### IV.4 Results

With our catalog of matched dark matter halos, we are able to directly compare differences in halo properties arising from initialization with 2LPT vs ZA. We consider halos on a pair-by-pair basis as well as the entire sample as a whole and in different mass bins. Overall, while we find a fair amount of agreement between 2LPT and ZA simulations, we do find an overall trend for 2LPT halos to be slightly ahead in their time evolution than their ZA counterparts, specifically in terms of mass, concentration, and relaxation.

We compare halo pairs on an individual halo-by-halo basis by eye for several of the most massive halos. Morphologies appear to be fairly similar for most halos, indicating good halo matches between simulations. However, for galaxies undergoing a major merger, the 2LPT halo mergers appear to often be slightly “ahead” of their ZA counterparts, appearing with a smaller nuclear separation in the case of dual nuclei or even lacking a noticeable second nucleus, while the ZA merger is still in progress. For an example halo pair with offset merger epochs, see Figure IV.1. The 2LPT halo seems to be in a nearly post-merger state, with an elongated but singular nucleus, while the ZA halo has two distinct major components.

Expanding this to an analysis of the halo population as a whole, we consider the central position offset  $X_{\text{off}}$ , defined as the distance between the halo density peak and the halo center-of-mass (Behroozi et al., 2013). In Figure IV.2, we plot histograms of the normalized difference in  $X_{\text{off}}$  between halos in the 2LPT and ZA simulations

$$\Delta X_{\text{off}} = \frac{X_{\text{off},2\text{LPT}} - X_{\text{off},\text{ZA}}}{X_{\text{off},\text{avg}}} \quad (\text{IV.2})$$

for three different redshifts and fit the data with generalized normal distributions also accounting for skew and kurtosis. Here, and likewise in subsequent histogram fits, we exclude the central bin at  $\Delta X_{\text{off}} = 0$  from the fit, measuring only the halo pairs with a non-negligible parameter displacement. The gray-shaded histogram counts only the halos in the top 25% mass quartile. We note that the mean  $\Delta X_{\text{off}}$  remains negative throughout the simulations, indicating a consistent trend for ZA halos to be less relaxed than their 2LPT counterparts for a given timestep.

In Figure IV.3, we plot histograms of the normalized mass difference

$$\Delta M_{\text{vir}} = \frac{M_{\text{vir},2\text{LPT}} - M_{\text{vir},\text{ZA}}}{M_{\text{vir},\text{avg}}} \quad (\text{IV.3})$$

in the left column, and histograms of the normalized concentration difference

$$\Delta c = \frac{c_{2\text{LPT}} - c_{\text{ZA}}}{c_{\text{avg}}} \quad (\text{IV.4})$$

in the right column for the same time steps as Figure IV.2.

From a high redshift, we find a tendency for 2LPT halos to be more massive, with larger halos contributing most to this difference. The positive mean and skew for the fit data are most evident at high redshift, with a decreasing trend approaching  $z = 6$ , where the distribution becomes more symmetrical than at higher redshift.

We see a similar trend for concentration. As with mass, 2LPT halos are more concen-

trated than their ZA companions, with the largest effect at high redshift. However, we do not observe the same amount of skew in the distributions at any redshift, and the most massive 25% of halos are much more evenly distributed about  $\Delta c = 0$  than the overall distribution. We also note that a central peak above the fit curve begins to appear in the histogram, becoming more pronounced toward later redshift, indicating a growing population of halos with little concentration difference between 2LPT and ZA simulations.

We consider  $\Delta M_{\text{vir}}$  and  $\Delta c$  as a function of average halo mass  $M_{\text{vir},2\text{LPT}} - M_{\text{vir},\text{ZA}}$  in Figure IV.4. The data is binned on a 2-D grid with a logarithmic color map for three representative timesteps. A linear fit to the data is overplotted in red, and a dotted blue line is provided at  $\Delta M_{\text{vir}} = 0$  and  $\Delta c = 0$  to guide the eye.

We find that  $\Delta M_{\text{vir}}$  tends to increase with increasing  $M_{\text{vir,avg}}$ , a trend that is, again, most pronounced at high redshift. 2LPT halos are consistently more massive than their ZA counterparts, with the difference increasing with average halo mass. While less massive halo pairs have a larger spread in the difference in 2LPT and ZA mass, more massive halo pairs are more consistently heavier in 2LPT than in ZA. The slope of the fit line trends towards zero as we progress in redshift, with little average mass dependence by  $z = 6$ .

The picture is less clear for concentration. We find a small trend for more massive halo pairs to be more concentrated in ZA, but this trend is weaker than for  $\Delta M_{\text{vir}}$ . The data have a larger variance than  $\Delta M_{\text{vir}}$ , and fits have an overall shallower slope. Mass dependence all but disappears by  $z = 6$ .

To more quantitatively assess the time progression of our various trends, see Figure IV.5, where we plot the mean, standard deviation, skew, and kurtosis of the fitting distributions for  $\Delta X_{\text{off}}$ ,  $\Delta M_{\text{vir}}$ , and  $\Delta c$  as a function of redshift in the left column, and the slopes of the fits for Figure IV.4 in the right column. (Talk about fits to fits and trends with redshift here for Figure IV.5.)

## IV.5 Discussion

As we evolve our DM halo population from our initial redshift to  $z = 6$ , we find a number of trends and implications. Simulation initialization with 2LPT can have a large effect on halo population compared to initialization with ZA. The second order displacement boost of 2LPT provides a head start on the initial collapse and formation of DM halos. This head start manifests itself structurally further along in a halo's evolution as potentially earlier mergers, and a more relaxed core for a given timestep following a merger event. 2LPT halos are, on average, more massive and more concentrated than their ZA counterparts. The larger mass for 2LPT halos is more pronounced for higher mass pairs, while 2LPT halo concentration is larger on the small mass end. Both mass and concentration differences trend towards symmetry about zero as halos evolve in time, with the smallest difference observed at the end of the simulations at  $z = 6$ . Casual extrapolation of our observed trends with redshift to today would indicate that 2LPT and ZA would produce very similar halo populations by  $z = 0$ . However, the larger differences at high redshift can have important consequences.

The use of 2LPT for simulation initialization could have significant effects in various areas. 2LPT simulations can be started at a later initial redshift, saving computation time and reducing numerical noise effects of smooth low density regimes. Many simulations are begun at too late a redshift for the size of box being simulated<sup>[citation needed]</sup>, a problem which could be greatly reduced by initialization with 2LPT. Additionally, the earlier formation times and larger masses of 2LPT halos could have important implications with respect to early halo life during the Dark Ages. Earlier forming, larger halos could affect the formation of Pop-III stars, and cause super-massive black holes (SMBHs) to grow more rapidly during their infancy. The epoch of peak star formation may also be shifted earlier. This could additionally affect the contribution of SMBHs and early star populations to re-ionization. Larger halos may also influence abundance matching studies.

We note a few caveats with our simulations and analysis. We did not exclude sub struc-

ture when determining the properties of a halo. Halo matching is not perfect, as it is based on one snapshot at a time, and may miss count halos due to merger activity and differences in merger epochs. However, we believe this effect to be minor. While we compared ROCKSTAR’s output with our own fitting routines and found them to be in good agreement, ROCKSTAR does not provide goodness of fit parameters for its NFW profile fitting and  $R_s$  measurements. It may be debated whether it makes sense to even consider concentration of halos at high redshift which are not necessarily fully virialized.

We use a simulation box size of only 10 Mpc. This is too small to effectively capture very large outlier density peaks. We would, however, expect these large uncaptured peaks to be affected the most by 2LPT initialization. Additionally, a larger particle number would allow us to consider smaller mass halos than we were able to here, and to better resolve all existing structure. A higher starting redshift could probe the regime where 2LPT initialization contributes the most. It would also be of interest to evolve our halo population all the way to  $z = 0$ . The addition of baryons in a fully hydrodynamical simulation could also affect halo properties. These may all be address in an upcoming set of simulations and follow-up paper.

## IV.6 Conclusion

We analyzed three 2LPT and ZA simulation pairs and tracked the spherical overdensity dark matter halos therein with the 6-D phase space halo finder code ROCKSTAR to compare the effect of initialization technique on properties of particle-matched dark matter halos. This approach allowed us to directly compare matching halos between simulations and isolate the effect of using 2LPT over ZA. In summary, we found the following:

- 2LPT halos get a head start in the formation process and are often caught in a later stage of merging than their ZA counterparts. This leads to merging ZA halos often appearing with a larger nuclear separation, more tidal features, and smaller masses than 2LPT halos for a given snapshot.

- 2LPT halos are, on average, more massive than ZA halos. Earlier collapse of the largest initial density peaks causes this effect to be most pronounced for the most massive halos.
- Halo concentration, likewise, is higher for 2LPT halos than ZA halos. However, halo pairs shift to more concentrated ZA halos in the high mass regime.
- Differences in nuclear displacement, mass, and concentration between 2LPT and ZA halos are most pronounced for high redshift. Halo population mass and concentration difference distributions, especially, begin settling toward symmetry by the end of the simulations.

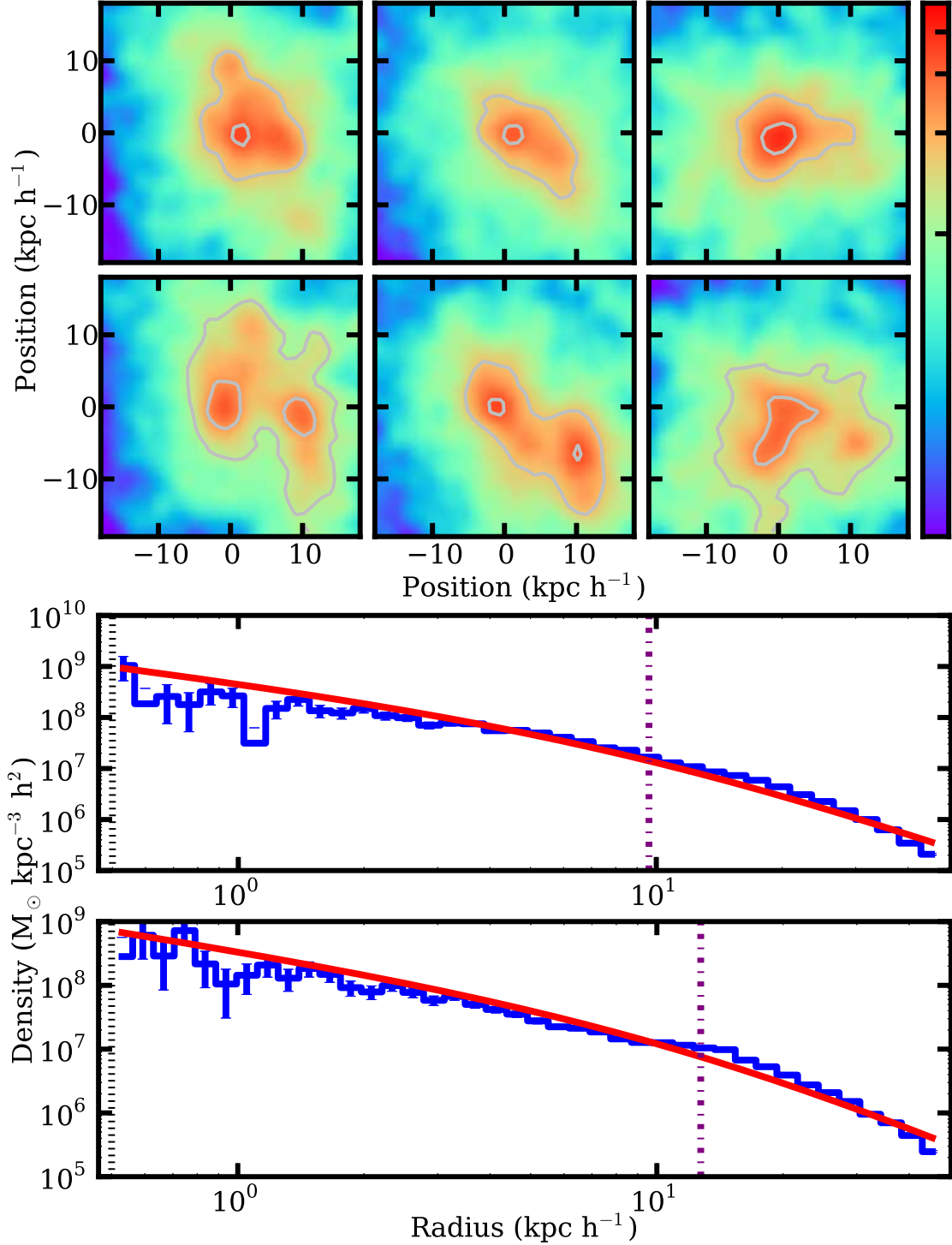
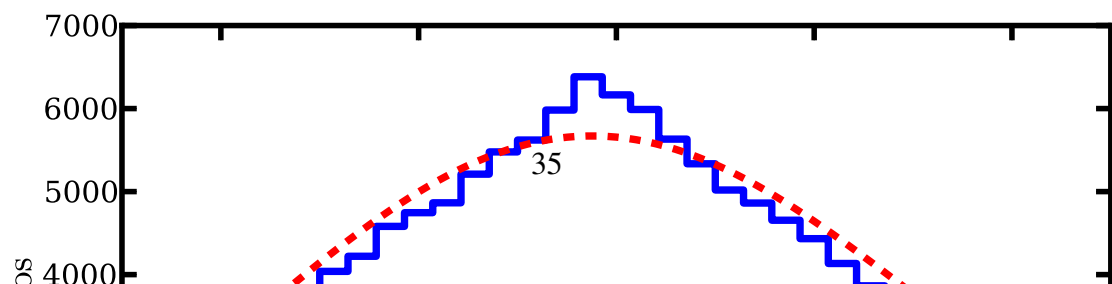
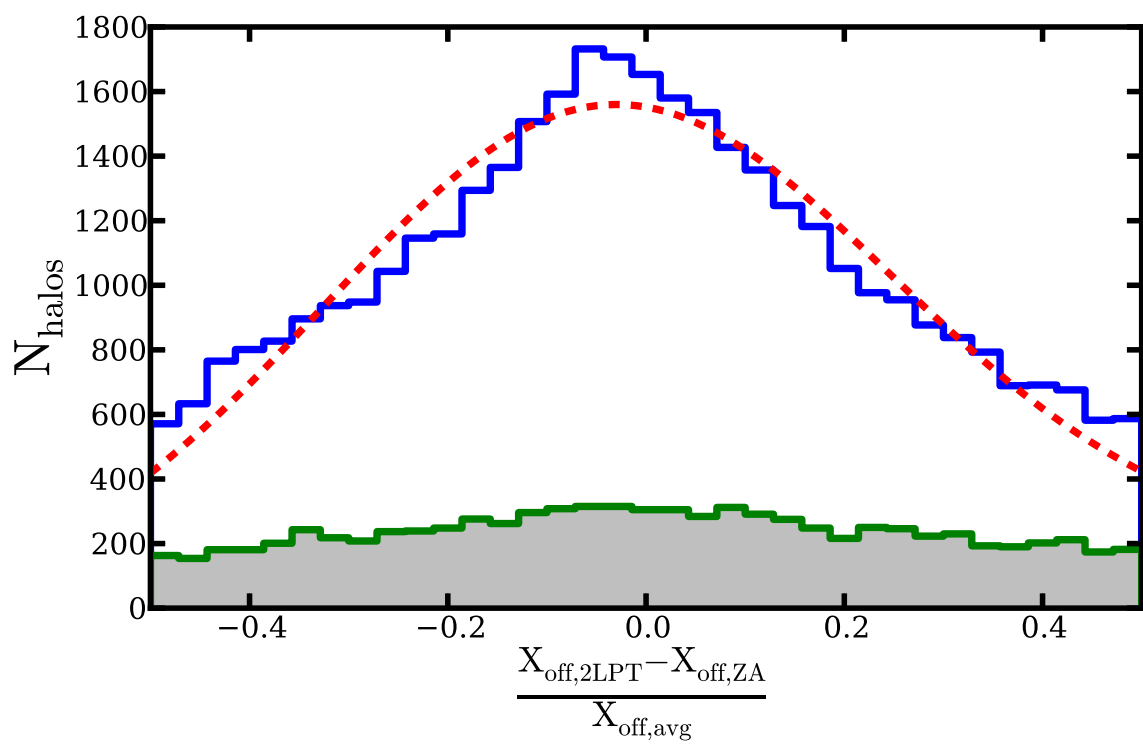
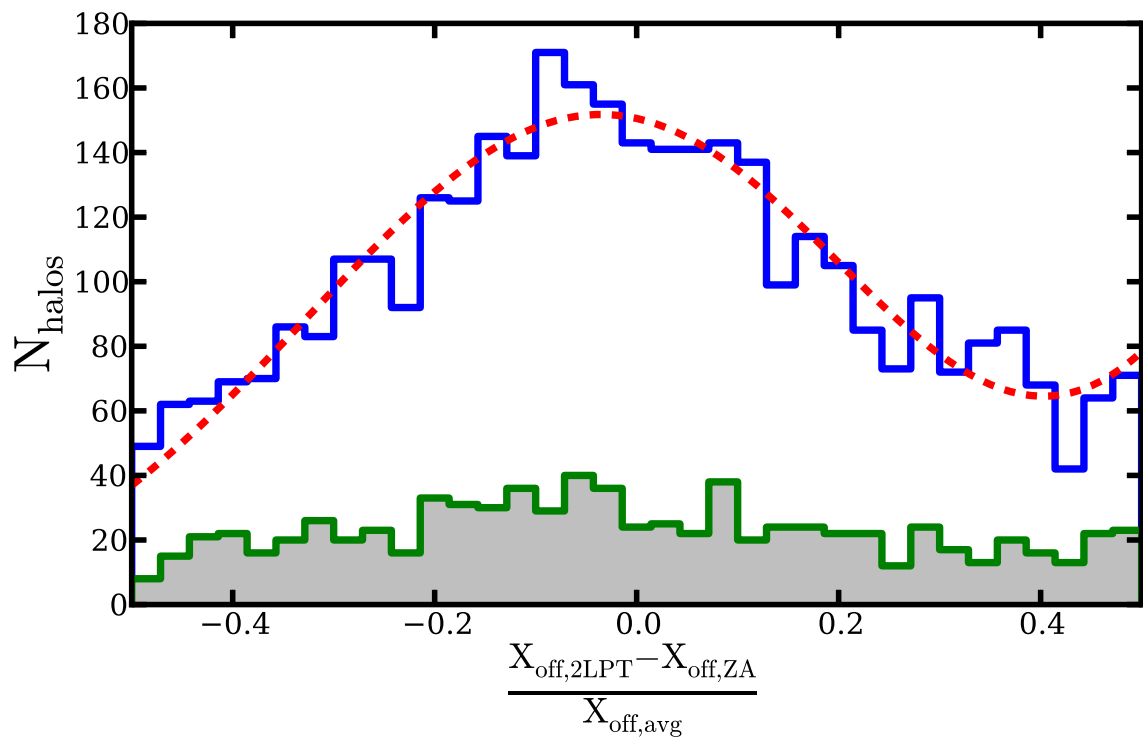


Figure IV.1: *Top two rows: Zoom in on nuclei?* Density projections for two matching halos at  $z = 6$ . The first and second row are 2LPT and ZA, respectively. Each halo is either undergoing or has just undergone a merger. The 2LPT halo appears to be further along in the merger process, while the ZA halo lags behind, still displaying two distinct cores. *Bottom two rows:* Density profiles for the same two halos as above. Logarithmic bins of radial particle position are fit to an NFW profile. The purple dot-dash line marks the scale radius. With nearly identical virial radii, the higher concentration of the 2LPT halo can be seen from its smaller scale radius. The black dotted line is the resolution limit of the simulations.





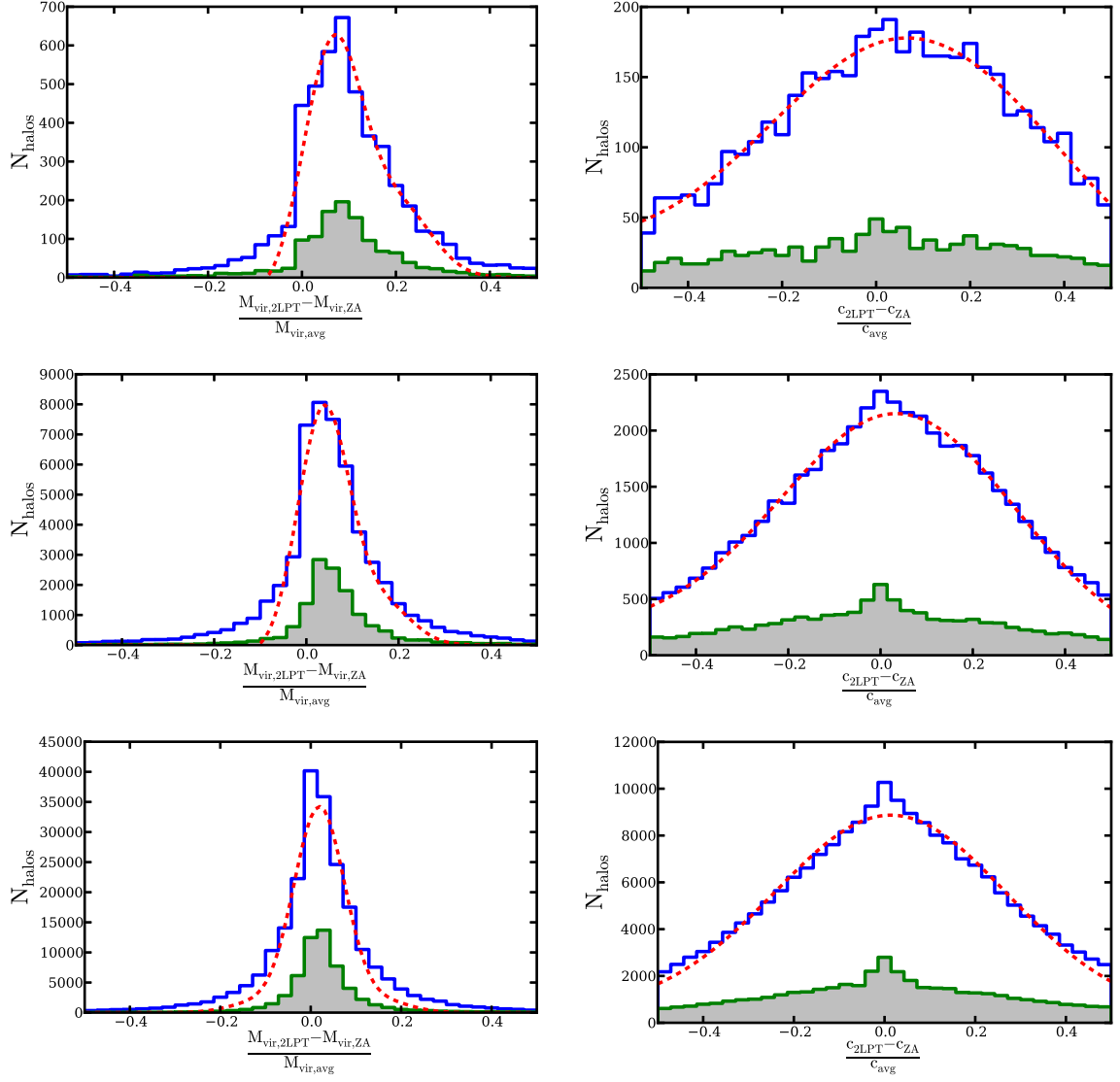


Figure IV.3: Like Figure IV.2, but for histograms of  $\Delta M_{\text{vir}}$  in the left column and  $\Delta c$  in the right column. Again, the top, middle, and bottom rows correspond to snapshots at  $z = 14.7$ ,  $z = 10.3$ , and  $z = 6.0$ , respectively, and generalized normal distributions fit to the data, excluding the central bin, are overplotted with a red dashed line.

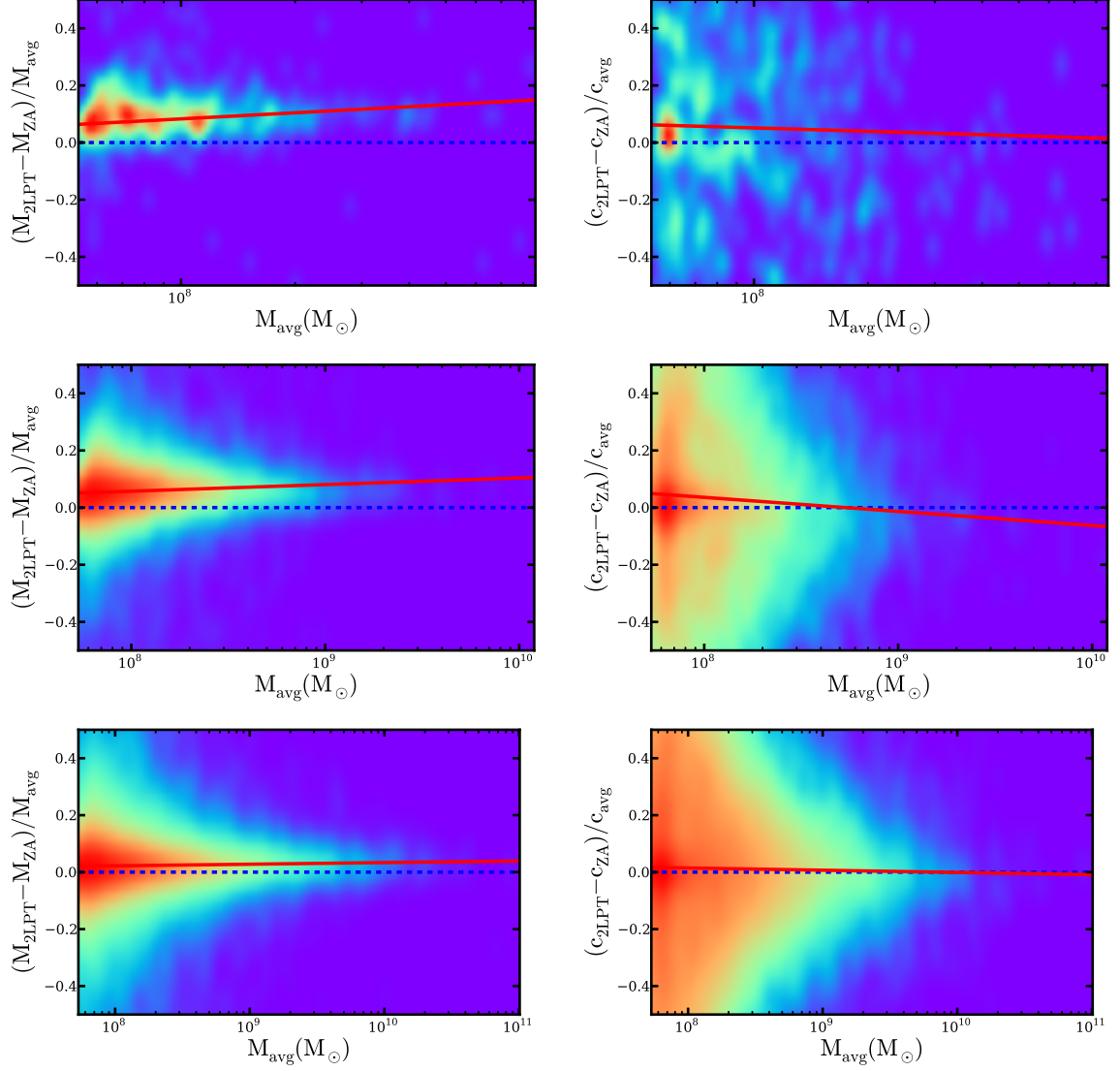


Figure IV.4:  $\Delta M_{\text{vir}}$  (left column) and  $\Delta c$  (right column) as a function of  $M_{\text{vir,avg}}$ . Halos are counted in 2-D rectangular bins and smoothed with a Gaussian kernel with a logarithmic color scale. The red line is the least-squares best fit to the data. The blue dashed line at zero is provided to guide the eye. The three rows again correspond to snapshots at  $z = 14.7$ ,  $z = 10.3$ , and  $z = 6.0$ , respectively.

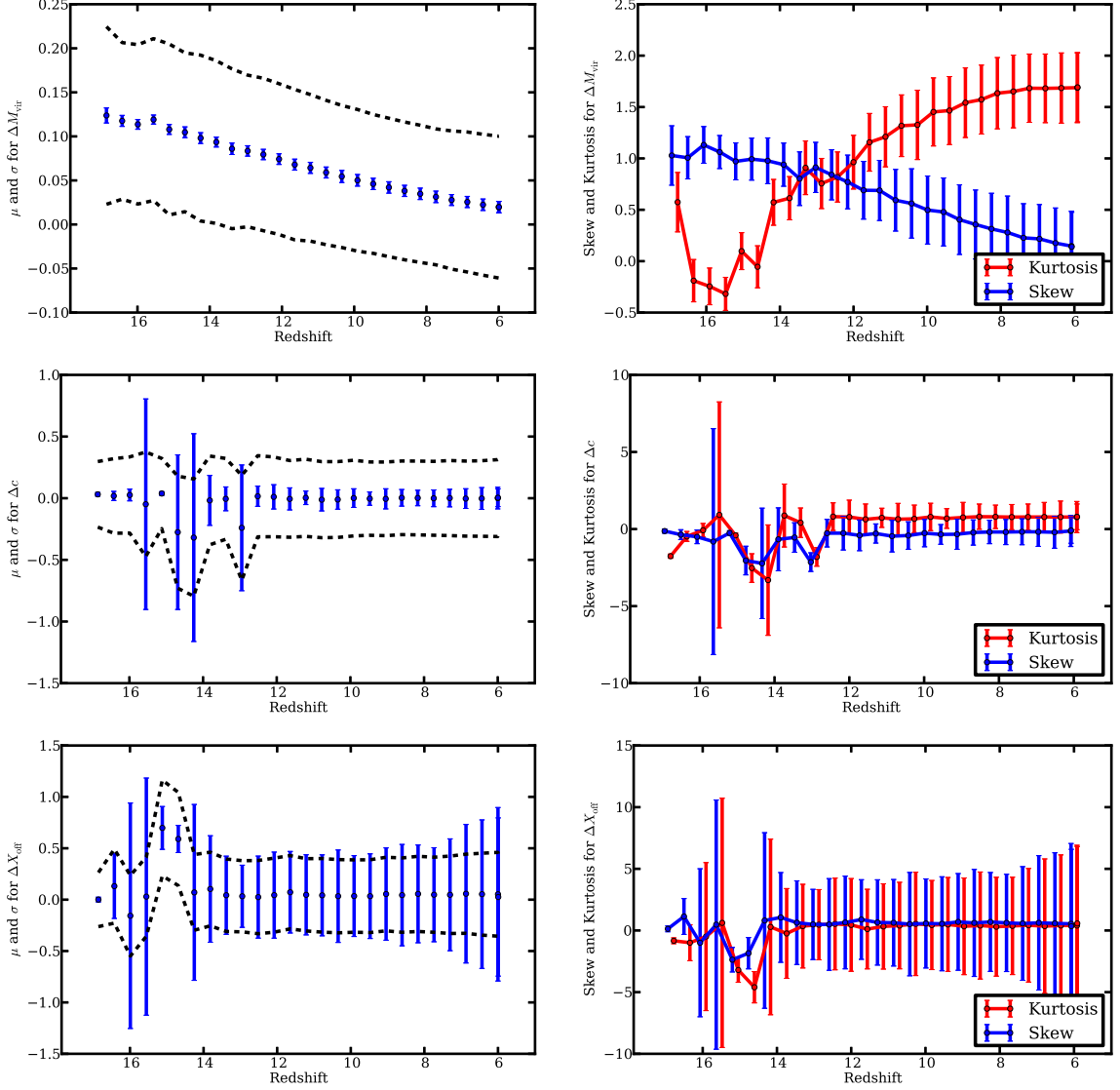


Figure IV.5: **Expand caption.** *Left column:* Mean and standard deviation (top panel), and skew and kurtosis (bottom panel) of the generalized normal distribution fits as a function of redshift for histograms in Figure IV.2 and Figure IV.3. In the top panel, the points have been offset slightly from each other in redshift to avoid overlap. *Right column:* Slope of fits as a function of redshift for  $\Delta M_{vir}$  (top panel) and  $\Delta c$  (bottom panel) from Figure IV.4.

## **CHAPTER V**

### **Conclusion**

## BIBLIOGRAPHY

- Behroozi, P. S., Wechsler, R. H., & Wu, H.-Y. 2013, *Astrophys. J.*, 762, 109
- Binney, J., & Merrifield, M. 1998, *Galactic Astronomy*, Princeton Series in Astrophysics (Princeton University Press)
- Binney, J., & Tremaine, S. 1988, *Galactic Dynamics*, Princeton Series in Astrophysics (Princeton University Press)
- Blandford, R. D., & McKee, C. F. 1982, *Astrophys. J.*, 255, 419
- Bondi, H. 1952, *Mon. Not. R. Astron. Soc.*, 112, 195
- Bondi, H., & Hoyle, F. 1944, *Mon. Not. R. Astron. Soc.*, 104, 273
- Brügmann, B., Tichy, W., & Jansen, N. 2004, *Phys. Rev. Lett.*, 92, 211101
- Bryan, G. L., & Norman, M. L. 1998, *Astrophys. J.*, 495, 80
- Chandrasekhar, S. 1943, *Astrophys. J.*, 97, 255
- Djorgovski, S., & Davis, M. 1987, *Astrophys. J.*, 313, 59
- González, J. A., Sperhake, U., Brügmann, B., Hannam, M., & Husa, S. 2007, *Phys. Rev. Lett.*, 98, 091101
- Gültekin, K., Richstone, D. O., Gebhardt, K., et al. 2009, *The Astrophysical Journal*, 698, 198
- Herrmann, F., Hinder, I., Shoemaker, D., Laguna, P., & Matzner, R. A. 2007, *Astrophys. J.*, 661, 430
- Herrnstein, J. R., Moran, J. M., Greenhill, L. J., et al. 1999, *Nature*, 400, 539
- Holley-Bockelmann, K., Gültekin, K., Shoemaker, D., & Yunes, N. 2008, *Astrophys. J.*, 686, 829
- Holley-Bockelmann, K., Wise, J. H., & Sinha, M. 2012, *Astrophys. J., Lett.*, 761, L8
- Hoyle, F., & Lyttleton, R. A. 1939, *Proceedings of the Cambridge Philosophical Society*, 35, 405
- Hubble, E. P. 1926, *Astrophys. J.*, 64, 321
- Khan, F. M., Just, A., & Merritt, D. 2011, *Astrophys. J.*, 732, 89
- Koppitz, M., Pollney, D., Reisswig, C., et al. 2007, *Phys. Rev. Lett.*, 99, 041102
- Kormendy, J., & Djorgovski, S. 1989, *Ann. Rev. Astron. Astrophys.*, 27, 235

- Lin, D., & Papaloizou, J. 1996, *Annual Review of Astronomy and Astrophysics*, 34, 703
- Lo, K. Y. 2005, *Ann. Rev. Astron. Astrophys.*, 43, 625
- Navarro, J. F., Frenk, C. S., & White, S. D. M. 1997, *Astrophys. J.*, 490, 493
- Rubin, V. C., Ford, W. K. J., & Thonnard, N. 1980, *Astrophys. J.*, 238, 471
- Rybicki, G. B., & Lightman, A. P. 1979, *Radiative processes in astrophysics* / George B. Rybicki, Alan P. Lightman (Wiley, New York :), xv, 382 p. :
- Schawinski, K., Urry, C. M., Virani, S., et al. 2010, *The Astrophysical Journal*, 711, 284
- Scheel, M. A., Boyle, M., Chu, T., et al. 2009, *Phys. Rev. D*, 79, 024003
- Shima, E., Matsuda, T., Takeda, H., & Sawada, K. 1985, *Mon. Not. R. Astron. Soc.*, 217, 367
- Springel, V. 2005, *Mon. Not. R. Astron. Soc.*, 364, 1105